Floquet Interpretation of Attosecond RABBITT Traces

Matteo Lucchini*
Department of Physics, Politecnico di Milano, 20133 Milano, Italy and
Institute for Photonics and Nanotechnologies, IFN-CNR, 20133 Milano, Italy
(Dated: July 10, 2023)

Originally proposed for the temporal characterization of train of attosecond pulses, the reconstruction of attosecond beating by interference of two-photon transitions (RABBITT), has become a wide-spread, powerful technique, capable to capture ultrafast electron dynamics through an interferometric approach. Starting from the well-known strong-field approximation (SFA) description of a two-color photoelectron spectrum, here we develop a model that interprets a RABBITT trace as the interference of different Floquet ladder states generated in the continuum by a femtosecond infrared (IR) pulse after ionization by the attosecond radiation. In turn, this allowed us to develop an analytical model capable of predicting the amplitude and phase of the oscillating sidebands and mainbands while including the effect of non-standard interference paths and, in first approximation, of the finite IR pulse envelope. Our results thus suggest a way to extend the RABBITT model to higher intensities and beating frequencies, and disentangle different oscillating signals in a congested photoelectron spectrogram as the one associated with molecular targets.

I. INTRODUCTION

Alongside with attosecond streaking [1, 2], in the recent years the reconstruction of attosecond beating by interference of two-photon transitions (RABBITT) [3, 4] has established as a powerful technique capable to access electron dynamics [5, 6] in atoms [7], molecules [8], liquids [9] and solids [10]. Pioneering experiments have shown the capability of this interferometric approach to resolve the ultrafast processes which unfold during photoemission [11, 12], disclosing the effect of different kind of resonances [13–19], nuclear motion [20, 21], local potential profile [22], spacial field distribution [23], continuum-continuum transitions [24] and angular beatings [25, 26].

In a RABBITT experiment a train of attosecond pulses (APT) in the extreme-ultraviolet (XUV) spectral region and a delayed femtosecond infrared (IR) pulse are focused onto the target to induce a two-color photoemission process. When the two radiations overlap in time, two-color ionization paths that involve the absorption of one XUV photon and the absorption/emission of one IR photon can lead to the same electron final energy. As a result the amplitude of the associated photoemission probability oscillates with the relative delay between the APT and the IR pulse, and valuable information about the energy-dependent phase of the electron wave-packet is encoded in the oscillation phase[27]. In the standard implementation of the technique the IR intensity is kept relatively low (typically $I_{IR} \sim 10^{11}$ W/cm^2 [28]) in order to avoid ionization paths that involve more than one IR photon. If, on the one side, this assures a clear interpretation of the experimental data, one of the major strengths of RABBITT over other techniques like streaking [29], on the other side it limits the energy resolution with which the phase of the electron wave-packet is sampled and the IR intensity range that can be explored. While several approaches have been proposed to increase the energy sampling of the technique [13, 21, 30, 31], the possibility to exploit higher-order interference paths to increase the information redundancy in a RABBITT trace has been little pursued [32]. Starting from an approach similar to that reported in Ref. [33], in this work we will interpret a RABBITT trace in terms of interference of Floquet ladder states [34, 35] and develop an analytical form that can be used to extract time-delay information from all the interference paths, including those avoided in a standard RABBITT regime. We will show that while ionization paths involving more than one IR photon become relevant already at relatively low IR intensities, their effect can be accounted for.

This work is organized as follows: Sec. II presents the mathematical model we developed and its validation against numerical simulation based on the well-known strong-field approximation (SFA) formula [36]. In Sec. III we discuss the effect of the IR intensity on the RABBITT phases and the activation of higher order interference paths, while in Sec. IV we show how the model can be non-adiabatically extended to include the effect of a finite IR pulse envelope. Finally, the last section presents the conclusion.

II. MATHEMATICAL MODEL

Within SFA and in absence of atomic resonances [37, 38], the photoelectron spectra obtained by ionizing an atom of binding energy I_p with an XUV pulse, $E_x(t)$, and an opportunely delayed IR pulse described by a vector potential $A_{IR}(t)$, can be calculated as (atomic units are used hereafter) [36]:

$$S(\omega,\tau) = \left| \int_{-\infty}^{\infty} \chi(t-\tau) e^{i\phi(p,t)} e^{iI_p t} dt \right|^2 , \qquad (1)$$

* matteo.lucchini@polimi.it

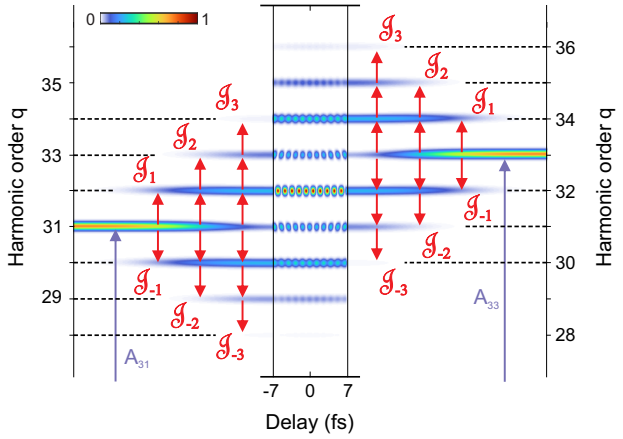

FIG. 1. Cartoon describing the interference (middle) between the Floquet ladder states associated to harmonic 31^{st} (left) and 33^{rd} (right) ionization in presence of a relatively strong IR field (7×10^{11} W/cm^2). Their coherent sum gives oscillating signals where the two ladder spectrally overlap.

where $\phi(p,t)$ is the quantum phase acquired by the electron emitted at the time instant t in the continuum due to the effect of the IR field,

$$\phi(p,t) = -\int_t^\infty \frac{1}{2}\left(p + A_{IR}(t')\right)^2 dt', \tag{2}$$

and the quantity $\chi(t)$ is the temporal electron wavepacket. It is given by the inverse Fourier transform of the product between the XUV spectrum, $\hat{E}_x(\omega)$, and the dipole matrix element which describes the transition from the ground state to the continuum [39]. This latter can be expressed in terms of the target photoionization cross-section amplitude $\sigma(\omega)$ and phase $\varphi_{at}(\omega)$ [11, 40], so that

$$\chi(t) = \mathcal{F}^{-1}\left\{\hat{E}_x(\omega)\sigma(\omega)e^{i\varphi_{at}(\omega)}\right\}. \tag{3}$$

Since the phase acquired during photoionization from a noble atom [41] is usually small when compared to the intrinsic chirp of the harmonic radiation (so called attochirp) [42], $\angle\{\hat{E}_x(\omega)\} \gg \varphi_{at}(\omega)$. Therefore, we can here consider only the effect of $\sigma(\omega)$ and impose $\varphi_{at}(\omega) = 1$ without losing generality.

If the IR pulses are long enough for the slowly varying envelope approximation (SVEA) to be valid, $\phi(p,t)$ can be expanded in a Fourier series [43] and the spectrogram of Eq. (1) can be rewritten as [33, 35]:

$$S(\omega,\tau) \simeq \left|\int_{-\infty}^{\infty} dt\chi(t-\tau) \times \sum_{n=-\infty}^{\infty} \mathcal{J}_n(\alpha,\beta)\, e^{i\left(\omega' - n\omega_0\right)t}\right|^2, \tag{4}$$

where $\alpha = {}^{-pE_0(t)}/_{\omega_0^2}$ and $\beta = {}^{-U_p(t)}/_{2\omega_0}$. Here $E_0(t) = E_0 g(t)$ is the IR field envelop, $E_{IR}(t) = {}^{-dA_{IR}(t)}/_{dt} = E_0(t)\sin(\omega_0 t)$ is the IR electric field, $\omega' = p^2/2 + U_p(t) + I_p$ is the photoelectron energy shifted by the target ionization potential and the instantaneous ponderomotive energy $U_p(t) = E_0^2(t)/(4\omega_0^2)$. $\mathcal{J}_n$ indicates the generalized Bessel function of order n, given by sum of products of ordinary Bessel functions J_j:

$$\mathcal{J}_n(x,y) = \sum_{j=-\infty}^{\infty} J_{n-2j}(x)J_j(y). \tag{5}$$

For monochromatic XUV and IR fields ($g(t) = 1$), Eq. (4) expresses the probability to ionize an atomic initial state of binding energy I_p, $|0\rangle = e^{iI_p t}\phi_0(\mathbf{r})$, with the XUV radiation and reach a Floquet(Volkov) state created by the IR field in the continuum [43, 44],

$$|\psi_V(t)\rangle = e^{-i\varepsilon t}\sum_{n=-\infty}^{\infty} \mathcal{A}_n e^{in\omega_0 t}|a_n\rangle, \tag{6}$$

where $|a_n\rangle$ are normalized spatial function, while the Floquet quasi-energy ε and the Floquet ladder amplitudes $\mathcal{A}_n$, are given by:

$$\begin{cases} \varepsilon = p^2/2 + U_p \\ \mathcal{A}_n = \mathcal{J}_n\left(-p\frac{E_0}{\omega_0^2}, -\frac{U_p}{2\omega_0}\right). \end{cases} \tag{7}$$

In this framework, each term $\mathcal{J}_n$ in Eq. (4) is thus linked to the probability to absorb/emit n IR photons, describing the creation of sidebands (SBs) above and below the main band (MB) associated to the direct XUV ionization into the continuum [45] (Fig. 1). The SB amplitude is directly linked to the amplitude of the Floquet ladder states created by the IR in the continuum $\mathcal{A}_n$ and this holds also for IR pulses that last only few optical cycles [35].

If we now assume that the XUV radiation is made of a perfect comb of odd harmonics with identical Gaussian envelope of width σ_e. The electron wavepacket in the frequency domain, $\hat{\chi}(\omega)$, can then be written as:

$$\hat{\chi}(\omega) = \sum_{\substack{q=0 \\ q,odd}}^{\infty} A_q e^{-\frac{\sigma_e^2}{2}(\omega - q\omega_0)^2} e^{i\varphi_q}, \tag{8}$$

where the quantities A_q and φ_q represent the spectral amplitude and phase of each harmonic (Fig. 2(a)), already rescaled by the target cross section $\sigma(\omega)$ (eventually including also the target phase φ_{at}). By considering only the short trajectories and neglecting any dependence over the radial profile, the harmonic phase (i.e. the attochirp) can be estimated with the following analytical formula [28]:

$$\varphi_q = \frac{\gamma}{I}\left(q - \frac{I_p}{\omega}\right)^2 \omega^2, \tag{9}$$

where $\gamma = 1.03 \times 10^{-18}$ s^{2}W/cm^2 for all gas targets and I is the laser intensity used to drive the harmonic generation (here set to 10^{14} W/cm^2). The attochirp calculated

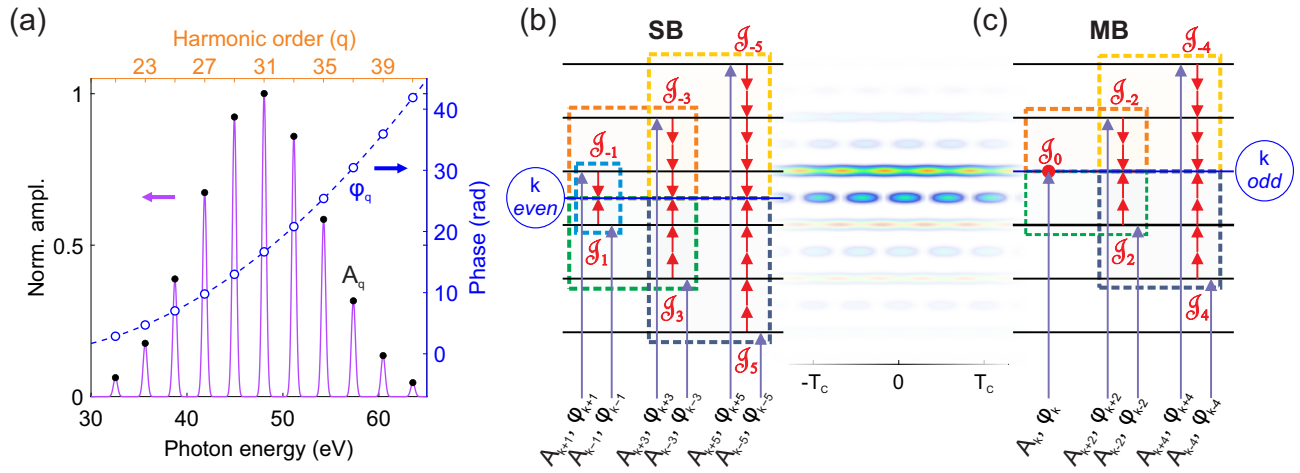

FIG. 2. **(a)** Spectral amplitude (solid violet) and phase (dashed blue) of the electron wavepacket generated by an attosecond pulse train in Ne. Black solid and blue open circles respectively mark the amplitude, A_q, and phase, φ_q of each harmonic contribution. Schematic of the mechanism that brings to the formation of the SB of even order k, **(b)**, and the mainband of odd order k (MB_k), **(c)**, considering up to the multiple absorption of 5 IR photons. The violet vertical arrows indicate the ionization by an harmonic of order $k+i$. The red arrows correspond to the absorption/emission of n IR photons coming from the n-th Floquet ladder state, whose probability scales with $\mathcal{J}_n$.

with Eq. (9) while considering harmonic generation in Ne ($I_p = 21.5646\,\mathrm{eV}$), is displayed by the blue dashed curve in Fig. 2(a).

If the bandwidth of each harmonic is narrow enough so that the final electron momentum p can be substituted with the central momentum p_k of each spectral feature ($k \in \mathbb{N}$, $k = q + n$),

$$p \to p_k = \sqrt{k\omega_0 - U_p - I_p},$$

the quantity α does not vary significantly within the harmonic bandwidth

$$\alpha \to \alpha_k = -p_k \frac{E_0(t)}{\omega_0^2},$$

and the spectrogram of Eq. (4) becomes a sum of Fourier transform:

$$S(\omega,\tau) \simeq \left| \sum_{n=-\infty}^{\infty} \mathcal{F}\left\{ \chi(t-\tau) \mathcal{J}_n\left(\alpha_k, \beta\right) e^{-in\omega_0 t} \right\} \right|^2 . \tag{10}$$

Under the assumption of a long IR pulse it is possible to factorize the time dependence in the generalized Bessel functions of Eq. (10) through the approximation $\mathcal{J}_n\left(\alpha_k, \beta\right) \simeq \mathcal{J}_n\left(\alpha_k^0, \beta^0\right) g(t)^{|n|}$, where $g(t) = 1$ is the IR pulse envelope, α_k^0 and β^0 are calculated using the peak field amplitude E_0 [35]. From the properties of the Fourier transform, it follows that

$$\mathcal{F}\left\{ \mathcal{J}_n\left(\alpha_k(t), \beta(t)\right) \right\} \to \mathcal{J}_n\left(\alpha_k^0, \beta^0\right) \delta(\omega),$$

and the spectrogram of Eq. (4) can thus be written as the coherent sum of replicas of the photoelectron spectrum, weighted by the coefficients $\mathcal{J}_n$ and shifted in energy by n IR photons:

$$S(\omega,\tau) \simeq \left| \sum_{n=-\infty}^{\infty} \mathcal{J}_n\left(\alpha_k^0, \beta^0\right) \hat{\chi}(\omega' - n\omega_0) e^{i\left(\omega' - n\omega_0\right)\tau} \right|^2 . \tag{11}$$

Finally, making use of definition of Eq. (8), $S(\omega,\tau)$ can be further rewritten has:

$$S(\omega,\tau) \simeq \left| \sum_{n=-\infty}^{\infty} \sum_{\substack{q=0 \\ q,odd}}^{\infty} \mathcal{J}_n\left(\alpha_k^0, \beta^0\right) A_q e^{-\frac{\sigma_e^2}{2}\left(\omega' - (q+n)\omega_0\right)^2} e^{i\varphi_q} e^{i\left(\omega' - n\omega_0\right)\tau} \right|^2 , \tag{12}$$

which corresponds to the coherent sum of all the Floquet ladder states associated to each harmonic of order q. As the intensity of the spectrogram around the final electron energy $\omega_k = p_k^2/2$ is given by the sum of all the addends which satisfy $q + n = k$, the formulation above allows an easy derivation of the expected harmonic (MB) and SB signals:

$$\mathrm{S}_k(\tau) \simeq \left| \sum_{\substack{n=-\infty \\ n,even/odd}}^{\infty} \mathcal{J}_n\left(\alpha_k^0, \beta^0\right) A_{k-n} e^{i\varphi_{k-n}} e^{-in\omega_0\tau} \right|^2 \tag{13}$$

where we have neglected the effect of the common harmonic envelope and the phase term $e^{i\omega'\tau}$. The integer n has the opposite parity of k. Odd values of k correspond to a MB while even values to a SB. Using the complex definition of the sinusoidal functions, $\mathrm{S}_k(\tau)$ can be rewritten as a sum of cosines oscillating at even multiples of the IR frequency ω_0. If m is an even, integer number, the term oscillating at $m\omega_0$ is thus given by:

$$S_k^{(m)}(\tau) = 2 \sum_{\substack{n=-\infty \\ n,even/odd}}^{\infty} \mathcal{J}_n\left(\alpha_k^0, \beta^0\right) A_{k-n} \mathcal{J}_{n-m}\left(\alpha_k^0, \beta^0\right) A_{k-n+m} \cos\left(m\omega_0\tau + \varphi_{k-n+m} - \varphi_{k-n}\right), \tag{14}$$

where n has the opposite parity of the chosen k. The above formula allows to predict the strength and phase of each frequency component constituting the SB/MB signal. Since, the sum of different cosine functions beating at the same frequency can be rewritten as:

$$\sum_n B_n \cos\left(x + \phi_n\right) = B\cos(x + \phi). \tag{15}$$

The amplitude and phase of each oscillatory component of $S_k(\tau)$ is thus given by:

$$\begin{cases} B^2 = \left(\sum B_n \cos\left(\phi_n\right)\right)^2 + \left(\sum B_n \sin\left(\phi_n\right)\right)^2 \\ \phi = \mathrm{atan2}\left(\sum B_n \sin\left(\phi_n\right), \sum B_n \cos\left(\phi_n\right)\right), \end{cases} \tag{16}$$

where

$$\begin{cases} B_n = \mathcal{J}_n\left(\alpha_k^0, \beta^0\right) A_{k-n} \mathcal{J}_{n-m}\left(\alpha_k^0, \beta^0\right) A_{k-n+m} \\ \phi_n = \varphi_{k-n+m} - \varphi_{k-n}. \end{cases} \tag{17}$$

For a chosen value of m, the summation of Eq. (14) can thus be rewritten as a single cosine whose amplitude and phase depend on the harmonic strengths A_i and the probability to exchange n IR photons at a given final electron energy $\mathcal{J}_n\left(\alpha_k^0, \beta^0\right)$, i.e. the Floquet ladder state amplitudes $\mathcal{A}_n$. Finally, if compared to a Fourier analysis of the SB signals, we note that Eq. (14) gives a deeper insight as it disentangles the cross-effect of the n-th order excitation paths in each $2m\omega_0$ component.

A. Sideband signal

For even values of k, the summation in Eq. (13) runs over the odd values of n and $S_k(\tau)$ describes a SB signal (Fig. 2(b)). It is given by the coherent sum of all the paths that lead to the same final electron energy ω_k. Therefore, besides the usual paths in RABBITT, i.e. the absorption of an XUV photon of energy $(k+1)\omega_0$ and the emission of one IR photon ($n = -1$) and the absorption of an XUV photon of energy $(k-1)\omega_0$ and the absorption of one IR photon ($n = 1$), all the other paths that involve an higher number of exchanged IR photons ($|n| > 1$) are considered. The relative strength of each path is determined by the relative harmonic amplitude A_{k-n} and the amplitudes of the Floquet ladder states $\mathcal{J}_n\left(\alpha_k^0, \beta^0\right)$. The phase of each frequency component of S_k can be evaluated with Eq. (14) with n odd. It is worth noticing, that while Eqs. (16) and Eqs. (17) suggest that, in general, the oscillating components of a SB depend on the IR intensity (through the terms $\mathcal{J}_n$) and the harmonic phase and strength (trough the φ_i and A_i), at low IR intensities $\mathcal{J}_n \to 0$ for $|n| > 1$, and the only photoionization paths that survive are the ones framed by the blue dashed box in Fig. 2(b). As a consequence, the SB signal is given by the interference of the first positive and negative Floquet ladder states of adjacent harmonics and it oscillates only with twice the IR frequency. $S_k^{(2)}(\tau)$, calculated with Eq. (14), gives the standard RABBITT formula

$$S_k^{(2)}(\tau) = 2\mathcal{J}_1 A_{k-1} \mathcal{J}_{-1} A_{k+1} \cos\left(2\omega_0\tau + \Delta\varphi_k\right), \tag{18}$$

where the oscillation phase corresponds to the difference between the phase of the adjacent harmonics $\Delta\varphi_k = \varphi_{k+1} - \varphi_{k-1}$, regardless the exact IR intensity and harmonic strength.

The stronger the IR intensity the more interfering paths do contribute to the total signal. As a result, more terms compete to the definition of $\mathrm{SB}_{2q}^{(2)}(\tau)$ (the colored rectangles in Fig. 2(b) indicate all the interfering

paths when processes involving up to 5 IR photons are considered), and the phase of the $2\omega_0$ component of the SB depends on I_{IR} and the spectral properties of other neighboring harmonics.

B. Harmonic signal

Odd values of k and even values of n in Eq. (13) describe an MB. Also in this case, the total signal is given by the interference of different ionization paths and its frequency components can be calculated with Eq. (14). At the low IR intensity limit, $S_k(\tau)$ (Fig. 2(c)) is proportional to $\mathcal{J}_0$ and it does not oscillate, corresponding to what expected in the RABBITT model and perturbation theory. With increasing IR intensity, the paths involving ladder states with $|n| = 2$ ($\mathcal{J}_{\pm 2}$, orange and green dashed boxes in Fig. 2(c)) become relevant and the MB signal oscillates with $2\omega_0$ as:

$$S_k^{(2)}(\tau) \propto \quad \left[\mathcal{J}_2 A_{k-2} \cos\left(2\omega_0\tau + \Delta\varphi_{0,-2}\right) + \right.$$
$$+ \quad \left. \mathcal{J}_{-2} A_{k+2} \cos\left(2\omega_0\tau + \Delta\varphi_{2,0}\right)\right] \qquad (19)$$

with $\Delta\varphi_{i,j} = \varphi_{k+i} - \varphi_{k+j}$. The $2\omega_0$ component of $S_k(\tau)$ thus behaves as $\propto \cos(2\omega_0\tau + \phi)$, where the phase ϕ contains information on the phase difference between the chosen harmonic and the adjacent ones, in a way that depends on the IR intensity, the harmonic strengths, and the Floquet ladder state amplitudes $\mathcal{J}_{\pm 2}$:

$$\tan(\phi) = \frac{\mathcal{J}_2 A_{k-2} \cos\left(\Delta\varphi_{0,-2}\right) + \mathcal{J}_{-2} A_{k+2} \cos\left(\Delta\varphi_{2,0}\right)}{\mathcal{J}_2 A_{k-2} \sin\left(\Delta\varphi_{0,-2}\right) + \mathcal{J}_{-2} A_{k+2} \sin\left(\Delta\varphi_{2,0}\right)}. \qquad (20)$$

The higher the IR intensity, the stronger the $\mathcal{J}_n$ terms with $|n| > 2$ become, and the more paths have to be included in the summation of Eq. (14), to evaluate $S_k^{(2)}$ (the boxes in Fig. 2(c) display the relevant paths considering Floquet ladder states with $|n| \leq 4$).

C. Comparison with the SFA model

Figure 3(a) shows a portion of a RABBITT trace calculated with the SFA formula of Eq. (1) assuming Ar as the atomic target. The electron wavepacket, $\hat{\chi}(\omega)$, is the same as in Fig. 2(a), generated in Ne with a linear attochirp obtained with Eq. (9). The IR pulse is centered around 800 nm, has a full-width half-maximum (FWHM) time duration of nine cycles ($9T_c \simeq 24$ fs) and a peak intensity, $I_{IR} = 9 \times 10^9$ W/cm^2. The horizontal lines in the left panel of Fig. 2(a) correspond to the direct harmonic ionization (MBs) while the weaker oscillating signals in between, visible only in the saturate colormap of Fig. 2(a)-right panel, are the SBs. To extract the SB and MB oscillation phase delay we integrated the spectrogram in a 0.4-eV wide energy window centered around the nominal transition values. To minimize the effect of the finite IR envelope the resulting delay-dependent signal is fitted with a function of the form $a\cos(2\omega_0\tau + b)$ while considering only the delay range $\tau \in [-T_c, T_c]$. The phase delay of the $2\omega_0$ component is then given by $\tau_i = b/2\omega_0$ with $i = SB$ or MB. The result for the SB signal, τ_{SB}, is marked by the black open circles in Fig. 3(b), while the MB phase delay, τ_{MB}, is shown by the blue open circles in Fig. 3(c).

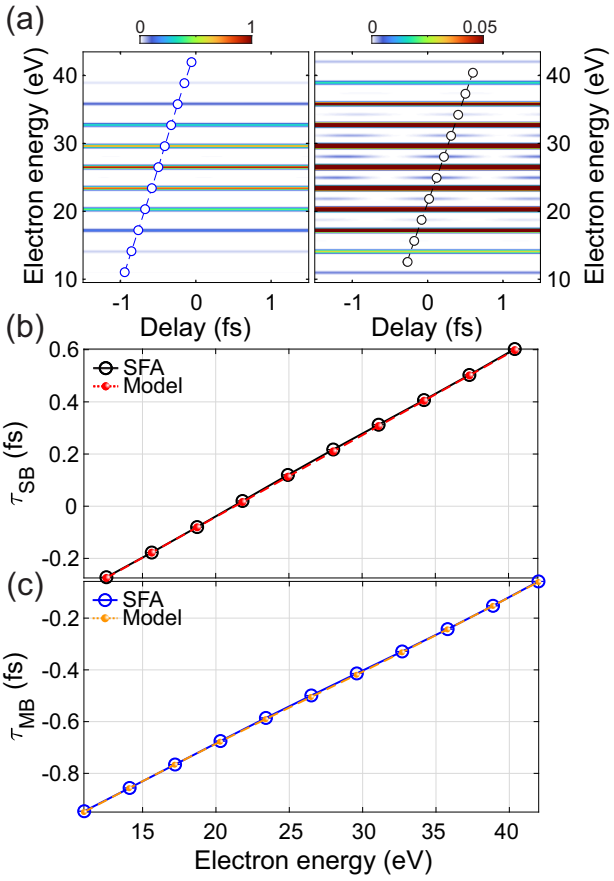

FIG. 3. **(a)** On the left: portion of a RABBITT trace simulated with the SFA formula of Eq. (1) and an IR intensity $I_{IR} = 10^9$ W/cm^2. On the right: same trace with saturated colors, showing the oscillating SB signals. The blue(black) open circles mark the SB(MB) delay $\tau_{SB}(\tau_{MB})$ extracted with a sinusoidal fit performed in the range $[-T_c, T_c]$. **(b)**, Comparison between the SB phase delay extracted from the SFA simulations in (a), black open circles, and the prediction of the Floquet-based model of Eq. (14), red full dots. **(c)**, Comparison between the MB phase delay as simulated with SFA (open blue circles) and calculated with the Floquet-based model (full orange dots).

The SB phase delays extracted from the SFA calculations are compared to the prediction of Eq. (14) (Fig. 3(b), red dots) showing a nice agreement. Due to the relatively low IR intensity, only the terms that depend on $\mathcal{J}_{\pm 1}$ survive in Eq. (14) and τ_{SB} can be fully explained with the standard RABBITT formula (Eq. (18)) which accounts only for one-IR photon processes. This

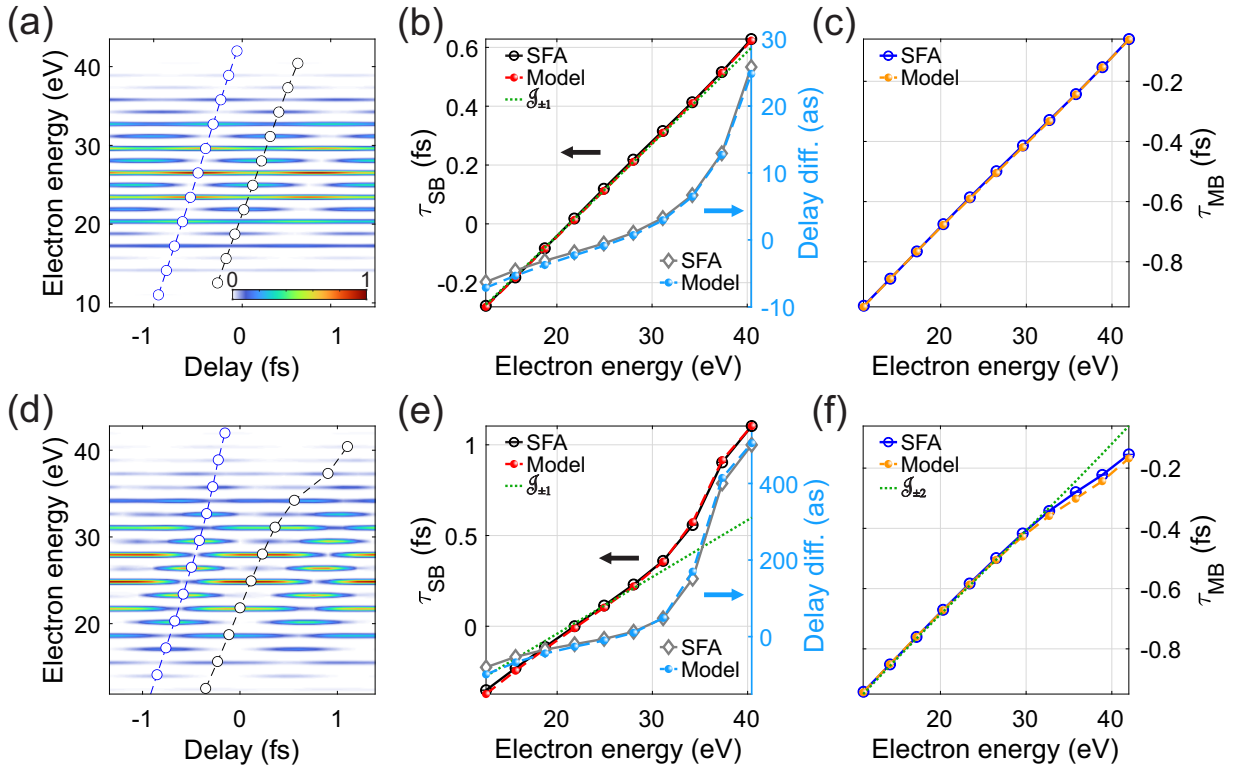

FIG. 4. **(a)** Portion of a RABBITT trace simulated with the SFA formula of Eq. (1) and an IR intensity $I_{IR} = 10^{11}$ W/cm^2. The blue(black) open circles mark the SB(MB) delay $\tau_{SB}(\tau_{MB})$ extracted with a sinusoidal fit performed in the range $[-T_c, T_c]$. **(b)**, **(c)**, Comparison between the phase delay extracted from the SFA simulations in (a), open circles, and the prediction of the Floquet-based model of Eq. (14), full dots, for the SB and MB signals, respectively. The open gray diamonds in (b) represent the deviation of the SFA results from the RABBITT model which accounts only for single-IR-photon processes (green dotted curve). This difference can be predicted with the model of Eq. (14) by including 3-IR photon processes, ($\mathcal{J}_{\pm3}$, full light-blue dots). **(d)-(f)**, Same as in (a)-(c) but for $I_{IR} = 7 \times 10^{11}$ W/cm^2. In this case a small deviation from the low-intensity regime of Eq. (19) ($\mathcal{J}_{\pm2}$, green dotted curve in (f)) is observed also in τ_{MB} because of 4-IR photon interactions ($\mathcal{J}_{\pm4}$).

underlines that, in this regime, the standard RABBITT analysis of the SB signals will produce the correct phase delays. Figure 3(c) compares τ_{MB} as extracted from the SFA calculations of Fig. 3(a) (open blue circles) with the prediction of Eq. (14) (orange dots). At these low IR intensities, only the paths governed by $\mathcal{J}_0$ and $\mathcal{J}_{\pm2}$ are relevant. As a result, the simulated τ_{MB} can be fully reproduced with Eq. (19), proving that the MB oscillation comes from the interference of ionization paths that involve the simultaneous absorption of two IR photons. This result validates the model of Eq. (14) for low IR intensities, suggesting a way to disentangle congested RABBITT traces where SBs and MBs of diverse order may energetically overlap [17, 46–49]. We note that the possibility of accounting for the amplitude of the oscillations and the phase of the MB signals goes beyond the standard RABBITT treatment, already at these low IR intensities.

III. DEPENDENCE ON THE IR INTENSITY

The model introduced in Sec. II allows us to investigate the effect of high-order IR processes (i.e., associated to the interference of ladder states with $|n| > 2$) in shaping the SB and MB phases. Figure 4(a) shows a portion of a RABBITT trace calculated as in Fig. 3(a) but for $I_{IR} = 10^{11}$ W/cm^2, a typical value used in RABBITT experiments [3]. Besides a stronger SB signal, also the MBs display clear oscillations in this case. The phase of this latter (open blue circles in Fig. 4(c)) can be fully reproduced with Eq. (19) (orange dots in Fig. 4(c)), showing that the MB oscillations originates from the interference of transitions with $n = 2$. The SB phase delay, (black open circles in Fig. 4(b)) starts instead to deviate from the RABBITT formula of Eq. (18) (green dotted curve). The difference between the two (gray open diamonds, right vertical axis) is of the order of few tens of attoseconds and can be recovered by including the terms with $|n| = 3$ in Eq. (14) and using Eqs. (16) and (17) to extract the phase delay (red and light-blue dots in Fig. 4(b)). We note that this delay difference expresses the error that one

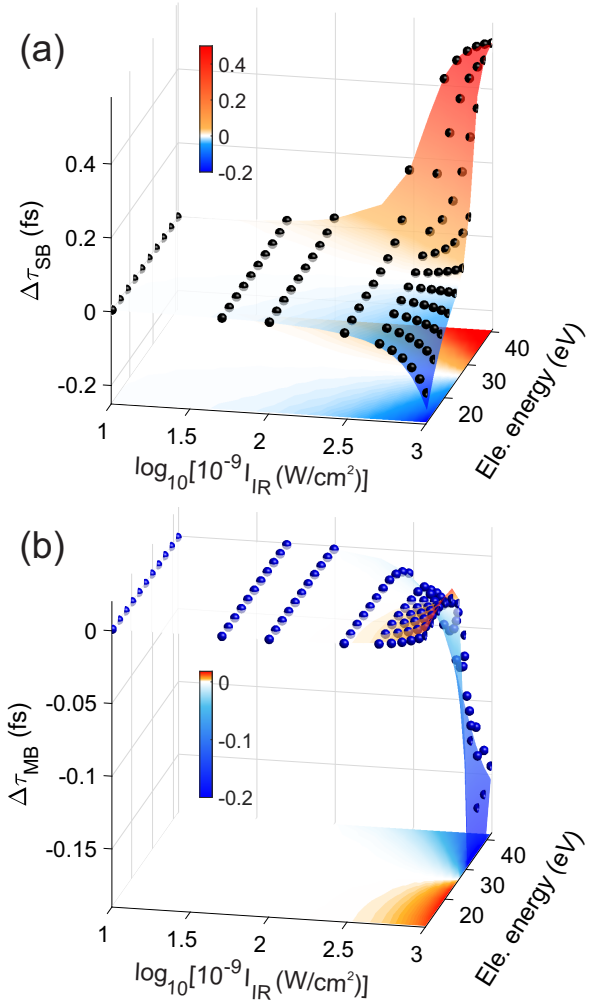

FIG. 5. **(a)** Difference between the phase delay of the $2\omega_0$ component of the SB signal extracted from the SFA calculations and the phase delay expected from processes that involve only the absorption/emission of one IR photon (classical RABBITT phase delay, Eq. (18)). The black dots are extracted from the SFA numerical simulations as a function of the SB energy and the IR intensity. The colored surface, projected in false colors onto the xy plane, represents the prediction of the Floquet-based analytical model, Eqs. (16) and (17). **(b)** Difference between the phase delay of the $2\omega_0$ component of the MB signal extracted from the SFA calculations and the phase delay expected from processes that involve only the absorption/emission of two IR photons (Eq. (19)). The blue dots are extracted from the SFA numerical simulations. The colored surface, projected in false colors onto the xy plane, represents the prediction of the Floquet-based analytical model.

would make by analyzing the spectrogram with a standard RABBITT approach. Even if, at these intensities, the error is of the order of tens of attosecond, it could be not negligible when evaluating small photoemission delays.

The higher I_{IR} the stronger the contribution of high order Floquet ladder states and the more the phase delay of the $2\omega_0$ oscillations deviates from the RABBITT formula of Eq. (18). Figure 4(d) shows a portion of RABBITT trace calculated with an IR intensity of 7×10^{11} W/cm^2. The SB and MB signals oscillate with more than one frequency component. Moreover, τ_{SB} and τ_{MB} (open markers in Figs. 4(e) and 4(f)) deviate from what predicted by Eqs. (18) and (19) (green dotted curve in Figs. 4(e) and 4(f)). While the behavior of τ_{MB} can be explained by including 4-IR photon processes in Eq. (14), n up to 5 has to be considered in the summation in order to recover the correct τ_{SB}.

The difference between the phase delay extracted from the SFA calculations and what predicted by Eqs. (18) and (19) gives a direct insight on the growing effect of IR multiphoton transitions (high-order Floquet ladder states) and the possible error introduced by applying the standard RABBITT analysis. The full dots in Fig. 5 present the difference between the SFA results and Eqs. (18), named $\Delta\tau_{SB}$ (panel (a)), and the difference between the SFA results and (19), $\Delta\tau_{MB}$ (panel (b)), for different values of the IR intensity in the range between 10^9 and 10^{12} W/cm^2. The colored surface represent the same quantity as calculated with the analytical model of Eq. (14). Despite the relatively high IR intensity challenges some of the approximations upon which the model is based, we found it to nicely reproduce $\Delta\tau_{SB}$ and $\Delta\tau_{MB}$ in the whole range under consideration. This is true not only for the $2\omega_0$ component, but also for the other frequency components, described by $m > 2$ in Eq. (14).

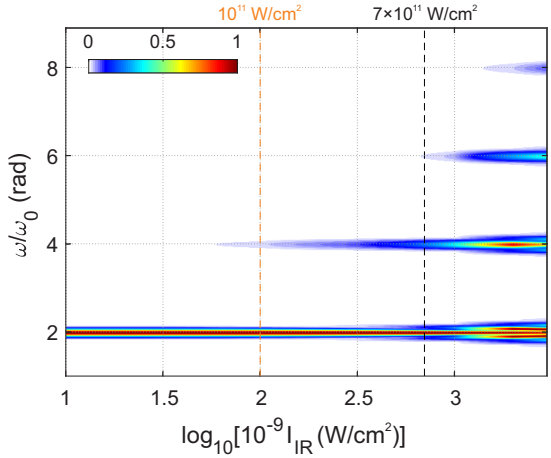

FIG. 6. Sum of the spectral power of the MB and SB signals composing a RABBITT trace as a function of the IR peak intensity I_{IR}. Each column is normalized by the intensity of the $2\omega_0$ component. The dashed orange and black lines mark the intensities used for the traces reported in Figs. 4(a) and 4(d), i.e. 1 and 7×10^{11} W/cm^2, respectively. While at low IR intensities, only a peak at $2\omega_0$ is present, components that oscillate at higher even multiples of ω_0 become appreciable for $I_{IR} \gtrsim 5 \times 10^{11}$ W/cm^2.

The results reported in Fig. 5 show that the devia-

tion from the low intensity limit (i.e. the standard RABBITT regime) can be important (up to hundreds of as for $I_{IR} \sim 10^{12}\,\mathrm{W/cm^2}$). Moreover, as 3-photon processes are enough to cause a non-zero $\Delta\tau_{SB}$ while 4-photon processes are necessary for $\Delta\tau_{MB}$, the SB phase delay deviates earlier from the expected RABBITT phase. As a rule of thumbs, if no $4\omega_0$ is observed the spectrogram is considered to be in the standard RABBITT regime where only the first order Floquet ladder states contribute. Each column in the color plot of Fig. 6 corresponds to the total spectral power of all SBs and MBs composing a RABBITT trace for a given I_{IR}. At a fix intensity, this is evaluated by performing a line-by-line Fourier transform of the SFA spectrogram along the delay axis, followed by a sum of the square modulus along the electron energy axis. A non-zero $4\omega_0$ component is observed at the IR intensity used for the calculations in Fig. 4(d) (vertical black dashed line in Fig. 6) confirming that one could use a simple argument to predict a deviation from the RABBITT regime in this case. At the IR intensity used for the calculations of Fig. 4(a) (vertical orange dashed line in Fig. 6), instead, no appreciable $4\omega_0$ component is observed in the total power spectrum. Nevertheless, both the results of Fig. 4(a) and of Fig. 5(a) show that the effect of the high-order processes cannot be neglected. Indeed, we found that $\Delta\tau_{SB} \neq 0$ already for $I_{IR} \sim 10^{11}\,\mathrm{W/cm^2}$, while $\Delta\tau_{MB}$ differs from zero for about $I_{IR} \sim 3 \times 10^{11}\,\mathrm{W/cm^2}$. This underlines: (1) an higher sensitivity of the $2\omega_0$ phase delay to the presence of multiphoton IR paths, proving that a simple argument based on the presence of higher components in the SB spectral power is not always enough, and (2) that the applicability of the standard RABBITT formula at moderate IR intensities ($\sim 10^{11}\,\mathrm{W/cm^2}$) may not be always justified, especially if the focus of the experiment is on small photoemission delays.

It is important to stress that the exact magnitude and energy-dependence of $\Delta\tau_{SB}$ and $\Delta\tau_{MB}$ do not only depend on the IR intensity, but also on the exact spectral shape of the harmonic radiation (φ_i) and the spectral harmonic strengths (A_i). A non-linear XUV chirp (caused for example by different focusing of the harmonics or by the transmission through a metallic filter) can produce a non-negligible $\Delta\tau_{SB}$ at lower I_{IR}. Finally, since amplitude of the Floquet ladder states scales as $\mathcal{J}_n\left(\alpha_k^0, \beta^0\right)$ with $\alpha_k^0 = -p_k E_0/\omega_0^2$, the actual final photoelectron momentum also affects the strengths of the transitions. As a result, the higher p_k, the lower the IR intensity needed to activate high-order processes. It follows that the error introduced by evaluating the SB phase delays with the standard RABBITT formula can be relevant also at the moderate IR intensities, routinely used in real experiments.

IV. EFFECT OF THE FINITE PULSE ENVELOPE

The model presented in the previous sections is developed for the case of long IR pulses which can be considered to be almost monochromatic. Nevertheless, RABBITT experiments are at times performed with relatively short pulses (10-20 fs) where the IR envelope $E_0 g(t)$ may have an influence. Given the dependence on I_{IR} dis-

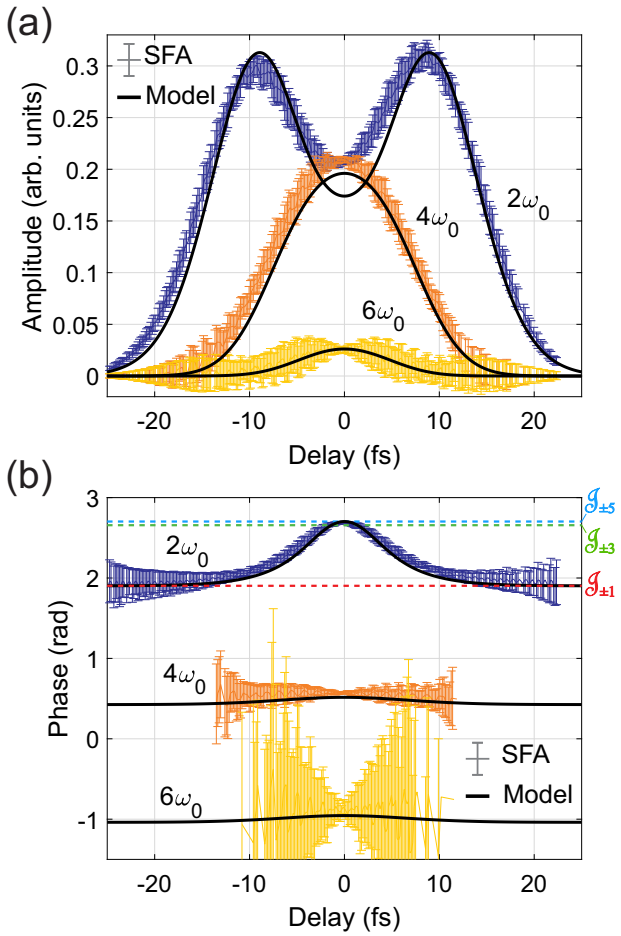

FIG. 7. **(a)** Amplitude of the different frequency components extracted from the sideband of order 36 (electron energy about 34.3 eV), generated with $I_{IR} = 7 \times 10^{11}\,\mathrm{W/cm^2}$ (same as Fig. 4(d)). The amplitudes extracted from the SFA data as described in the main text are reported with the colored curves. The error bars represent the confidence interval of the fitting procedure used. The full black curves represent instead the prediction of the Floquet-based model which accounts for the instantaneous IR intensity. **(b)** Phase of the different spectral components of SB_{36} as extracted from the SFA calculations (colored curves with error bars). The solid black curves represent the prediction of the Floquet-based model. The dashed lines mark the phase expected for the $2\omega_0$ component when processes involving the simultaneous absorption/emission of 1 ($\mathcal{J}_{\pm1}$ in red), 3 ($\mathcal{J}_{\pm3}$ in green), and 5 ($\mathcal{J}_{\pm5}$ in light-blue) are considered.

cussed in Sec. III, we expect that for high peak intensities, both the spectral components of a SB/MB signal and their phase delay will change along the RABBITT trace following the instantaneous IR intensity profile. To investigate this phenomenon we extracted the delay profile of $S_{36}(\tau)$ by integrating the spectrogram of Fig. 4(d) in a 0.4-eV wide window centered at 34.3 eV (nominal value of the electron kinetic energy). The resulting signal is multiplied with a rectangle of width equal to an IR optical period (T_c) prior being fitted with a function of the form

$$f(\tau) = \sum_{i=1}^{3} a_i \cos\left(2i\omega_0\tau - b_i\right).$$

The resulting amplitudes (a_i) and phases (b_i) extracted with this fitting procedure while sliding the rectangular window across the entire delay axis are displayed with the colored curves in Figs. 7(a) and 7(b), respectively. The error bars indicate the confidence interval of the fits. At relatively big negative and positive delays, when the local IR intensity is weak, the $S_{36}(\tau)$ oscillates with a $2\omega_0$ component (dark blue curves) whose phase can be predicted by Eq. (14) considering only those transitions that involve the exchange of a single IR photon ($\mathcal{J}_{\pm1}$, red dashed line in Fig. 7(b)). the lower the modulus of the delay, $|\tau|$, the stronger the local IR intensity and the SB signal exhibits a growing $4\omega_0$ (orange curves) and $6\omega_0$ (yellow curves) components which peak at $\tau = 0$ fs. As a result, the terms with $|n| > 1$ cannot be neglected in the computation of $S_{36}^{(2)}(\tau)$ and its phase changes, mostly because 3-IR photon processes ($\mathcal{J}_{\pm3}$, green dashed line in Fig. 7(b)), reaching the expected value ($\mathcal{J}_{\pm5}$, light-blue dashed line) around delay zero. One way to investigate the evolution of the spectral amplitudes and phase within the IR pulse envelope is to compute the Fourier transforms of Eq. (10) while including the explicit time-dependence of the $\mathcal{J}_n$ through α_k and β. Nevertheless, an analytical solution is possible only if the IR pulse envelope can be described by a well-behaving function (e.g. a Gaussian bell) for which the integrals can be solved. A less rigorous approach consists in substituting α_k^0 and β^0 in Eq. (14) with the same quantities calculated using the local IR envelope amplitude: $\alpha_k(\tau) = \alpha_k^0 g(\tau)$ and $\beta(\tau) = \beta^0 g(\tau)^2$. The results, plotted in Fig. 7 as solid black curves, nicely follow the delay-dependence of both amplitude and phase of the different frequency components of the SB signal. Despite the crude non-adiabatic approximation, if the IR intensity is not too high (i.e. $I_{IR} \lesssim 10^{12}\,\mathrm{W/cm^2}$) our model is thus able to correctly predict the evolution of the SB and MB signals along the spectrogram.

CONCLUSION

Starting from the SFA description of the two-color spectrogram generated by attosecod radiation and fs IR pulses, we have developed an alternative formulation based on the Fourier decomposition of the IR-dependent phase term. In case of relatively long IR pulses (quasi-monochromatic), this allowed us to show that the spectrogram originates from the interference of Floquet ladder states of the continuum (Volkov states) or, equivalently, from the interference of replicas of the attosecond radiation spectrum shifted in energy by integer multiples of the IR photon. If the attosecond radiation is in the form of a train of pulses, the spectrogram is composed by discrete peaks, SBs and MBs, whose amplitude oscillates along the delay axis. The model we propose allows an analytical derivation of those signals, which assume the form of a sum of cosine functions, oscillating with even multiples of the IR frequency ω_0. Our results show that both the amplitude and phase of the different frequency components depend on the spectral properties of the XUV radiation, the IR intensity and the electron final momentum. We have tested the prediction of the model against SFA numerical simulations, proving its capability to describe the amplitude and phase of the oscillations in an IR intensity range between 10^9 and $10^{12}\,\mathrm{W/cm^2}$.

At the weak IR limit ($I_{IR} < 10^{11}\,\mathrm{W/cm^2}$), in agreement with second-order perturbation theory at the basis of the well-known RABBITT model, the SBs are given by the interference of two-color ionization paths involving only one IR photon. As a result, the SB phase delay depends only on the phase of the adjacent harmonics and not on their amplitude. At higher IR intensities, ionization paths involving Floquet ladder states with $|n| > 2$ become relevant affecting both the amplitude and phase of the SB oscillations. Interestingly, we found this to produce a deviation from the RABBITT model already for IR intensities of the order of $10^{11}\,\mathrm{W/cm^2}$ where a simple inspection of the SB power spectrum will reveal no appreciable high frequency components. Being of the order of few tens of as, the effect of the additional interfering paths is not relevant if RABBITT is used to reconstruct the average attosecond pulse in the train, but it can hinder a proper retrieval of small photoemission delays if not properly accounted for.

Since the phase delay of the MBs always depends on the strength of both the involved harmonics and IR induced transitions, these signals are usually ignored in a RABBITT analysis. Our model provides an analytical expression to evaluate the amplitude and phase of the MBs, showing that they contain valuable information on the harmonic phase. The availability of an analytical prediction for the MB signals is important as: (*i*) it allows their analysis, increasing the statistics and robustness associated to a standard RABBITT trace, and (*ii*) it proves crucial for case of congested traces generated by ionizing a molecular target characterized by more then one initial state. Indeed, in this condition often SBs and MBs of different order and different initial state overlap in final energy. The total electron yield is given by their incoherent sum, hindering a direct evaluation of the RABBITT phase delay. If combined with a proper calibration of the

IR intensity at target and an accurate measurement of the XUV-only photoelectron spectrum (to get the A_q), the model we proposed can be used to perform a simultaneous non-linear fit of the spectrogram and disentangle overlapping SB and MB signals, thus extending the applicability of RABBITT to congested traces.

Finally, we show that a non-adiabatic extension of the model can be used to correctly retrieve the phase and amplitude of the spectral components of SB and MB signals also for the case of finite IR pulses. While the results and analytical formulas here presented are strictly valid within the SFA approximation and under the assumption of a pure free-electron final state (Volkov wave), the general approach can be applied to all those cases where the electron final state is dressed by the IR field so that the related wavefunction can be expanded in Fourier series following the Floquet theory. The mathematical formulas will depend on the exact problem under scrutiny, but their interpretation in terms on interference of Floquet ladder state will still hold.

By describing RABBITT traces from a different perspective, our results not only allow an interpretation of RABBITT phase delays, including higher order effects, but they also set the basis for the extension of the technique to congested spectrograms and higher IR intensities. While this latter regime is normally avoided, our work shows that it may be worthy to explore as a deviation from the presented model can be ascribed to IR-induced modifications of photoemission itself, possibly suggesting new ways to gain optical control on this fundamental process on sub-fs time scales.

ACKNOWLEDGMENTS

This project has received funding from the European Research Council (ERC) under the European Union's Horizon 2020 research and innovation programme (grant agreement No. 848411 title AuDACE) and from MIUR FARE PHorTUNA, Grant No. R209LXZRSL. The author wish to acknowledge fruitful scientific discussion with Dr. Rocío Borrego-Varillas and Prof. Mauro Nisoli.

[1] J. Itatani, F. Quéré, G. L. Yudin, M. Y. Ivanov, F. Krausz, and P. B. Corkum, Attosecond Streak Camera, Physical Review Letters **88**, 173903 (2002).

[2] Y. Mairesse and F. Quéré, Frequency-resolved optical gating for complete reconstruction of attosecond bursts, Physical Review A **71**, 011401(R) (2005).

[3] P. M. Paul, Observation of a Train of Attosecond Pulses from High Harmonic Generation, Science **292**, 1689 (2001).

[4] H. Muller, Reconstruction of attosecond harmonic beating by interference of two-photon transitions, Applied Physics B **74**, s17 (2002).

[5] F. Krausz and M. Ivanov, Attosecond physics, Reviews of Modern Physics **81**, 163 (2009).

[6] R. Borrego-Varillas, M. Lucchini, and M. Nisoli, Attosecond spectroscopy for the investigation of ultrafast dynamics in atomic, molecular and solid-state physics, Reports on Progress in Physics **85**, 066401 (2022).

[7] K. Klünder, J. M. Dahlström, M. Gisselbrecht, T. Fordell, M. Swoboda, D. Guénot, P. Johnsson, J. Caillat, J. Mauritsson, A. Maquet, R. Taïeb, and A. L'Huillier, Probing single-photon ionization on the attosecond time scale, Phys. Rev. Lett. **106**, 143002 (2011).

[8] F. Kelkensberg, W. Siu, J. F. Pérez-Torres, F. Morales, G. Gademann, A. Rouzée, P. Johnsson, M. Lucchini, F. Calegari, J. L. Sanz-Vicario, F. Martín, and M. J. J. Vrakking, Attosecond control in photoionization of hydrogen molecules, Physical Review Letters **107**, 043002 (2011).

[9] I. Jordan, M. Huppert, D. Rattenbacher, M. Peper, D. Jelovina, C. Perry, A. von Conta, A. Schild, and H. J. Wörner, Attosecond spectroscopy of liquid water, Science **369**, 974 (2020).

[10] R. Locher, L. Castiglioni, M. Lucchini, M. Greif, L. Gallmann, J. Osterwalder, M. Hengsberger, and U. Keller, Energy-dependent photoemission delays from noble metal surfaces by attosecond interferometry, Optica **2**, 405 (2015).

[11] R. Pazourek, S. Nagele, and J. Burgdörfer, Attosecond chronoscopy of photoemission, Reviews of Modern Physics **87**, 765 (2015).

[12] M. Isinger, R. J. Squibb, D. Busto, S. Zhong, A. Harth, D. Kroon, S. Nandi, C. L. Arnold, M. Miranda, J. M. Dahlström, E. Lindroth, R. Feifel, M. Gisselbrecht, and A. L'Huillier, Photoionization in the time and frequency domain, Science **358**, 893 (2017).

[13] V. Gruson, L. Barreau, Á. Jiménez-Galan, F. Risoud, J. Caillat, A. Maquet, B. Carré, F. Lepetit, J.-F. Hergott, T. Ruchon, L. Argenti, R. Taïeb, F. Martín, and P. Salières, Attosecond dynamics through a fano resonance: Monitoring the birth of a photoelectron, Science **354**, 734 (2016).

[14] M. Huppert, I. Jordan, D. Baykusheva, A. von Conta, and H. J. Wörner, Attosecond Delays in Molecular Photoionization, Physical Review Letters **117**, 093001 (2016).

[15] C. Cirelli, C. Marante, S. Heuser, C. L. M. Petersson, Á. J. Galán, L. Argenti, S. Zhong, D. Busto, M. Isinger, S. Nandi, S. Maclot, L. Rading, P. Johnsson, M. Gisselbrecht, M. Lucchini, L. Gallmann, J. M. Dahlström, E. Lindroth, A. L'Huillier, F. Martín, and U. Keller, Anisotropic photoemission time delays close to a Fano resonance, Nature Communications **9**, 955 (2018).

[16] Z. Tao, C. Chen, T. Szilvási, M. Keller, M. Mavrikakis, H. Kapteyn, and M. Murnane, Direct time-domain observation of attosecond final-state lifetimes in photoemission from solids, Science **353**, 62 (2016).

[17] L. Kasmi, M. Lucchini, L. Castiglioni, P. Kliuiev, J. Osterwalder, M. Hengsberger, L. Gallmann, P. Krüger, and U. Keller, Effective mass effect in attosecond electron

transport, Optica **4**, 1492 (2017).
[18] J. Riemensberger, S. Neppl, D. Potamianos, M. Schäffer, M. Schnitzenbaumer, M. Ossiander, C. Schröder, A. Guggenmos, U. Kleineberg, D. Menzel, F. Allegretti, J. V. Barth, R. Kienberger, P. Feulner, A. G. Borisov, P. M. Echenique, and A. K. Kazansky, Attosecond dynamics of *sp*-band photoexcitation, Phys. Rev. Lett. **123**, 176801 (2019).
[19] X. Gong, W. Jiang, J. Tong, J. Qiang, P. Lu, H. Ni, R. Lucchese, K. Ueda, and J. Wu, Asymmetric attosecond photoionization in molecular shape resonance, Phys. Rev. X **12**, 011002 (2022).
[20] L. Cattaneo, J. Vos, R. Y. Bello, A. Palacios, S. Heuser, L. Pedrelli, M. Lucchini, C. Cirelli, F. Martín, and U. Keller, Attosecond coupled electron and nuclear dynamics in dissociative ionization of H 2, Nature Physics **14**, 733 (2018).
[21] L. Cattaneo, L. Pedrelli, R. Y. Bello, A. Palacios, P. D. Keathley, F. Martín, and U. Keller, Isolating attosecond electron dynamics in molecules where nuclei move fast, Phys. Rev. Lett. **128**, 063001 (2022).
[22] J. Vos, L. Cattaneo, S. Patchkovskii, T. Zimmermann, C. Cirelli, M. Lucchini, A. Kheifets, A. S. Landsman, and U. Keller, Orientation-dependent stereo Wigner time delay and electron localization in a small molecule, Science **360**, 1326 (2018).
[23] M. Lucchini, L. Castiglioni, L. Kasmi, P. Kliuiev, A. Ludwig, M. Greif, J. Osterwalder, M. Hengsberger, L. Gallmann, and U. Keller, Light-Matter Interaction at Surfaces in the Spatiotemporal Limit of Macroscopic Models, Physical Review Letters **115**, 137401 (2015).
[24] J. Fuchs, N. Douguet, S. Donsa, F. Martin, J. Burgdörfer, L. Argenti, L. Cattaneo, and U. Keller, Time delays from one-photon transitions in the continuum, Optica **7**, 154 (2020).
[25] S. Heuser, Á. Jiménez Galán, C. Cirelli, C. Marante, M. Sabbar, R. Boge, M. Lucchini, L. Gallmann, I. Ivanov, A. S. Kheifets, J. M. Dahlström, E. Lindroth, L. Argenti, F. Martín, and U. Keller, Angular dependence of photoemission time delay in helium, Physical Review A **94**, 063409 (2016).
[26] V. Loriot, A. Marciniak, G. Karras, B. Schindler, G. Renois-Predelus, I. Compagnon, B. Concina, R. Brédy, G. Celep, C. Bordas, E. Constant, and F. Lépine, Angularly resolved rabbitt using a second harmonic pulse, Journal of Optics **19**, 114003 (2017).
[27] J. Dahlström, D. Guénot, K. Klünder, M. Gisselbrecht, J. Mauritsson, A. L'Huillier, A. Maquet, and R. Taïeb, Theory of attosecond delays in laser-assisted photoionization, Chemical Physics **414**, 53 (2013).
[28] M. Isinger, D. Busto, S. Mikaelsson, S. Zhong, C. Guo, P. Salières, C. L. Arnold, A. L'Huillier, and M. Gisselbrecht, Accuracy and precision of the rabbit technique, Philosophical Transactions of the Royal Society A: Mathematical, Physical and Engineering Sciences **377**, 20170475 (2019).
[29] L. Cattaneo, J. Vos, M. Lucchini, L. Gallmann, C. Cirelli, and U. Keller, Comparison of attosecond streaking and RABBITT, Optics Express **24**, 29060 (2016).
[30] G. Laurent, W. Cao, H. Li, Z. Wang, I. Ben-Itzhak, and C. L. Cocke, Attosecond control of orbital parity mix interferences and the relative phase of even and odd harmonics in an attosecond pulse train, Phys. Rev. Lett. **109**, 083001 (2012).
[31] M. Kotur, D. Guénot, Á. Jiménez-Galán, D. Kroon, E. W. Larsen, M. Louisy, S. Bengtsson, M. Miranda, J. Mauritsson, C. L. Arnold, S. E. Canton, M. Gisselbrecht, T. Carette, J. M. Dahlström, E. Lindroth, A. Maquet, L. Argenti, F. Martín, and A. L'Huillier, Spectral phase measurement of a Fano resonance using tunable attosecond pulses, Nature Communications **7**, 10566 (2016).
[32] M. Swoboda, J. M. Dahlström, T. Ruchon, P. Johnsson, J. Mauritsson, A. L'Huillier, and K. J. Schafer, Intensity dependence of laser-assisted attosecond photoionization spectra, Laser Physics **19**, 1591 (2009).
[33] T. Ruchon and A. Camper, Notes on attosecond pulse profile measurements with the rabbit technique (EDP Sciences, 2013) p. 01014.
[34] S.-I. Chu and D. A. Telnov, Beyond the Floquet theorem: generalized Floquet formalisms and quasienergy methods for atomic and molecular multiphoton processes in intense laser fields, Physics Reports **390**, 1 (2004).
[35] M. Lucchini, F. Medeghini, Y. Wu, F. Vismarra, R. Borrego-Varillas, A. Crego, F. Frassetto, L. Poletto, S. A. Sato, H. Hübener, U. D. Giovannini, Ángel Rubio, and M. Nisoli, Controlling floquet states on ultrashort time scales, Nature Communications **13**, 7103 (2022).
[36] M. Kitzler, N. Milosevic, A. Scrinzi, F. Krausz, and T. Brabec, Quantum Theory of Attosecond XUV Pulse Measurement by Laser Dressed Photoionization, Physical Review Letters **88**, 173904 (2002).
[37] V. S. Yakovlev, J. Gagnon, N. Karpowicz, and F. Krausz, Attosecond streaking enables the measurement of quantum phase, Physical Review Letters **105**, 073001 (2010).
[38] R. Borrego-Varillas and M. Lucchini, Reconstruction of atomic resonances with attosecond streaking, Opt. Express **29**, 9711 (2021).
[39] H. Wei, T. Morishita, and C. D. Lin, Critical evaluation of attosecond time delays retrieved from photoelectron streaking measurements, Physical Review A **93**, 053412 (2016).
[40] M. Y. Ivanov, M. Spanner, and O. Smirnova, Anatomy of strong field ionization, Journal of Modern Optics **52**, 165 (2005).
[41] J. Mauritsson, M. B. Gaarde, and K. J. Schafer, Accessing properties of electron wave packets generated by attosecond pulse trains through time-dependent calculations, Physical Review A **72**, 013401 (2005).
[42] S. Kazamias and P. Balcou, Intrinsic chirp of attosecond pulses: Single-atom model versus experiment, Physical Review A **69**, 063416 (2004).
[43] L. B. Madsen, Strong-field approximation in laser-assisted dynamics, American Journal of Physics **73**, 57 (2005).
[44] D. M. Wolkow, Über eine Klasse von Lösungen der Diracschen Gleichung, Zeitschrift für Physik **94**, 250 (1935).
[45] B. Moio, G. L. Dolso, G. Inzani, N. Di Palo, R. Borrego-Varillas, M. Nisoli, and M. Lucchini, Time-frequency mapping of two-colour photoemission driven by harmonic radiation, Journal of Physics B: Atomic, Molecular and Optical Physics **54**, 154003 (2021).
[46] S. Haessler, B. Fabre, J. Higuet, J. Caillat, T. Ruchon, P. Breger, B. Carré, E. Constant, A. Maquet, E. Mével, P. Salières, R. Taïeb, and Y. Mairesse, Phase-resolved attosecond near-threshold photoionization of molecular

nitrogen, Physical Review A **80**, 011404(R) (2009).

[47] J. Caillat, A. Maquet, S. Haessler, B. Fabre, T. Ruchon, P. Salières, Y. Mairesse, and R. Taïeb, Attosecond resolved electron release in two-color near-threshold photoionization of n_2, Physical Review Letters **106**, 093002 (2011).

[48] I. Jordan and H. J. Wörner, Extracting attosecond delays from spectrally overlapping interferograms, Journal of Optics **20**, 024013 (2018).

[49] A. Kamalov, A. L. Wang, P. H. Bucksbaum, D. J. Haxton, and J. P. Cryan, Electron correlation effects in attosecond photoionization of co_2, Physical Review A **102**, 023118 (2020).